Hongping Hu[1]
Department of Mechanics;
Hubei Key Laboratory of Engineering Structural Analysis and Safety Assessment,
Huazhong University of Science and Technology,
Wuhan 430074, China;
Franche-Comté Electronique Mécanique Thermique et Optique, CNRS UMR 6174,
Université de Bourgogne Franche-Comté,
Besançon 25030, France
e-mail: huhp@hust.edu.cn

Longxiang Dai
Department of Mechanics;
Hubei Key Laboratory of Engineering Structural Analysis and Safety Assessment,
Huazhong University of Science and Technology,
Wuhan 430074, China

Hao Chen
Department of Mechanics;
Hubei Key Laboratory of Engineering Structural Analysis and Safety Assessment,
Huazhong University of Science and Technology,
Wuhan 430074, China

Shan Jiang
Department of Mechanics;
Hubei Key Laboratory of Engineering Structural Analysis and Safety Assessment,
Huazhong University of Science and Technology,
Wuhan 430074, China;
Franche-Comté Electronique Mécanique Thermique et Optique, CNRS UMR 6174,
Université de Bourgogne Franche-Comté,
Besançon 25030, France

Hairen Wang[1]
Purple Mountain Observatory,
Chinese Academy of Sciences,
Nanjing 210008, China
e-mail: hairenwang@pmo.ac.cn

Vincent Laude
Franche-Comté Electronique Mécanique Thermique et Optique, CNRS UMR 6174,
Université de Bourgogne Franche-Comté,
Besançon 25030, France

Two Methods to Broaden the Bandwidth of a Nonlinear Piezoelectric Bimorph Power Harvester

We propose two methods to broaden the operation bandwidth of a nonlinear pinned–pinned piezoelectric bimorph power harvester. The energy-scavenging structure consists of a properly poled and electroded flexible bimorph with a metallic layer in the middle, and is subjected to flexural vibration. Nonlinear effects at large deformations near resonance are considered by taking the in-plane extension of the bimorph into account. The resulting output powers are multivalued and exhibit jump phenomena. Two methods to broaden the operation bandwidth are proposed: The first method is to extend the operation frequency to the left single-valued region through optimal design. The second method is to excite optimal initial conditions with a voltage source. Larger output powers in the multivalued region of the nonlinear harvester are obtained. Hence, the operation bandwidth is broadened from the left single-valued region to the whole multivalued region. [DOI: 10.1115/1.4035717]

Keywords: piezoelectric power harvester, nonlinearity, multivalued region, jump phenomena

1 Introduction

Piezoelectric materials have been used to make various electromechanical transducers for a long time. In particular, polarized ferroelectric ceramics have been used for force or power handling devices including actuators and transformers, due to their strong piezoelectric coupling. Recently, operating some of these devices without a wired power source has become an important issue, because of the rapid development of wireless electronic devices in both civilian and military applications. One approach is to harvest energy from the operating environment. As small electronic devices with a very low power requirement, piezoelectric materials are natural candidates for making devices that can scavenge ambient energy by converting mechanical energy into electric energy [1]. Such a piezoelectric device is called piezoelectric generator, or power harvester, or energy harvester.

[1]Corresponding authors.

Contributed by the Technical Committee on Vibration and Sound of ASME for publication in the Journal of Vibration and Acoustics. Manuscript received June 17, 2016; final manuscript received January 6, 2017; published online April 13, 2017. Assoc. Editor: Miao Yu.

Linear piezoelectricity theory can be used to describe the basic behavior of piezoelectric structures. Basing on it, the dependence of the performance of piezoelectric power harvesters upon the structure and the electric circuit parameters has been extensively studied. When operated near resonance, the piezoelectric power harvester can convert most mechanical vibration energy into electrical energy, since relatively strong mechanical deformations are induced. However, nonlinear phenomena occur when a piezoelectric structure operates in the resonance region [2]. Therefore, it is crucial to predict the resonance behavior for the design of piezoelectric power harvesters. Because nonlinear effects are very often undesirable, a nonlinear analysis is required to determine the operating range of a power harvester. Nonlinear coupling between the piezoelectric structure and the storage circuit with a rectifier bridge has been studied [3,4]. Hu et al. [5] studied the nonlinear behavior of a piezoelectric harvester with a plate structure operating in thickness-shear vibration mode. Xue and Hu [6] studied the nonlinear behavior of a plate piezoelectric structure harvesting energy from axisymmetric vibration. Wang et al. [7,8] studied the nonlinearity of a piezoelectric circular plate supporting flexural modes. Nonlinear techniques have been proposed for broadband energy harvesting. Ramlan et al. [9] investigated the potential benefits of a nonlinear stiffness in an energy harvesting device by using a mass–spring–damper system. Magnetic nonlinearity was incorporated into a linear system to broaden its operating bandwidth [10,11]. Leadenham and Erturk [12] developed an M-shaped piezoelectric energy harvester configuration that can exhibit a nonlinear frequency response which offers a 660% increase in the half-power bandwidth as compared to the linear system. Yang et al. [13] proposed a compressive-mode piezoelectric energy harvester and developed an analytical model of the nonlinear mechanical and electrical behaviors of the system, taking into account nonlinear stiffness, nonlinear damping, and nonlinear piezoelectricity. Bistable energy harvesting devices comprising a piezoelectric cantilever beam or plate and an apparatus to impose axial force may be effective across a broad-frequency bandwidth [14–17]. However, one main challenge is to maintain high-energy orbits for maximum power harvesting performance [15]. Maintaining high-energy orbits somehow depends on the level of ambient vibration. To overcome the challenge, there exist several methods to push the system to the higher energy state: controlling the input displacement level, sweeping the frequency down then sweeping quasi-statically back up, changing a phase lag between the harvested frequency and a second controlled input frequency, etc.

In this work, we propose two methods to broaden the operation bandwidth of a pinned–pinned piezoelectric bimorph power harvester. The first method is to make the left single-valued frequency region wider by designing the parameters of the system. The second method is to impose actively a set of initial conditions to boost the output power within the multivalued region. The proposed bimorph vibrates with flexural motion coupled with in-plane extension. Ambient low-frequency vibrations contain abundant energy. A bimorph in deflection mode has a relatively low natural frequency and easily resonates from ambient vibrations [18]. The constitutive relations are derived, and the equilibrium and compatibility equations of a piezoelectric bimorph with flexural modes are established in Sec. 2. Nondimensionalization and the harmonic balance method are employed. The output power of a bimorph power harvester is obtained in Sec. 3. Two methods to broaden the operation bandwidth are demonstrated in Sec. 4, and a few conclusions are drawn in Sec. 5.

2 Analysis of a Piezoelectric Bimorph Power Harvester

As shown in Fig. 1, the structure of a pinned–pinned piezoelectric bimorph power harvester consists of a bimorph with a metallic layer in the middle. One layer of the bimorph is polarized along the thickness direction and the other layer is polarized with the opposite poling direction. Values for material constants and geometric parameters of the harvester are listed in Table 1. A concentrated mass is not introduced into the harvester since its effect on the harvester has been studied extensively [19–21]. The ambient vibration is simulated as a sinusoidal pressure with the driving frequency ω_0, uniformly acting on the surface of the piezoelectric layer. Two surfaces and two interfaces of the bimorph are covered by electrodes which are represented by thick lines. Fig. 1(*b*) shows the cross section A, and the electric load which is simplified by a resistor R. Because the energy-scavenging structure is pinned–pinned as shown in Fig. 1(*a*), it is not allowed to present any in-plane displacement at the two ends, $x_1 = 0$ and $x_1 = L$. Therefore, a coupled flexural-extension vibration is driven by the sinusoidal pressure.

According to the classical theory for coupled flexural and extensional vibrations of beams [22–24], the in-plane normal strain of the beam can be written as

$$S_1 = u_{1,1} + \frac{1}{2}u_{3,1}^2 - x_3 u_{3,11} \tag{1}$$

where $u_1(x_1, t)$ and $u_3(x_1, t)$ are the extensional and the flexural displacements of the neutral layer of the bimorph, respectively.

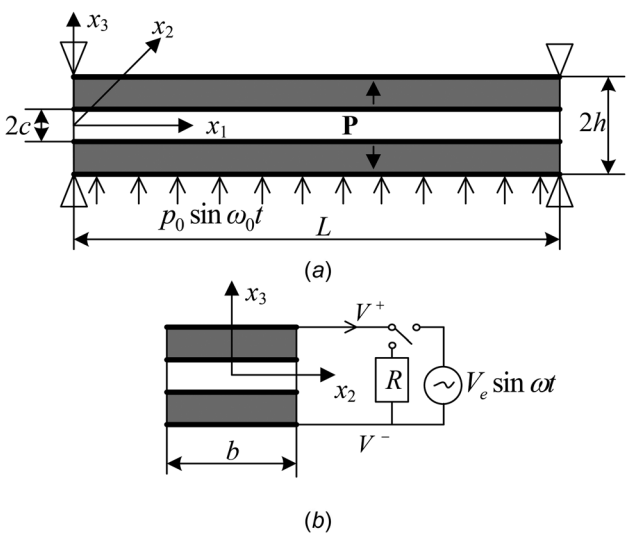

Fig. 1 A pinned-pinned piezoelectric bimorph power harvester: (*a*) front view and (*b*) side view of the structure

Table 1 Material constants and geometric properties of the harvester

Parameter, symbol	Value
Metal layer	
Young's modulus, E	70 GPa
Mass density, ρ	2700 kg/m^3
Length, L	100 mm
Width, b	8 mm
Thickness, 2c	0.4 mm
Piezoelectric layer	
Elastic compliance constant, s_{11}	16.5 m^2/N
Piezoelectric constant, d_{31}	-274×10^{-12} C/N
Dielectric constant, ε_{33}	3.01×10^{-8} C/(V·m)
Mass density, ρ'	7500 kg/m^3
Length, L	100 mm
Width, b	8 mm
Thickness, h-c	0.3 mm
Other	
Electric load, R	1 MΩ
Mechanical damping coefficient, ξ	0.003

These displacements are independent of x_2 and x_3. Subscripts 1 and 11 preceded by a comma denote the partial derivatives $\partial/\partial x_1$ and $\partial^2/\partial x_1^2$, respectively.

The electric voltages corresponding to the electrode configuration in Fig. 1(*b*) are denoted by V^+ for $x_3 = h$ and V^- for $x_3 = -h$ [7,25]. Superscripts "+" and "−" represent the top and bottom electrodes, respectively. The electrodes on the two interfaces of the bimorph are grounded as a voltage reference. The electric field in the ceramic layers corresponding to the electrode configurations, as shown in Fig. 1, has the following components:

$$E_1 = 0, \quad E_2 = 0, \quad E_3 = -\varphi_{,3} \tag{2}$$

where φ is the electrical potential across the piezoelectric layers. Only the axial stress is considered under the usual one-dimensional stress approximation of a beam [26,27]

$$T_1 = T_1(x_1, t) \tag{3}$$

Then, the relevant constitutive relations for the ceramic layers can be written as [28]

$$\begin{aligned} S_1 &= s_{11} T_1 + d_{31} E_3 \\ D_3 &= d_{31} T_1 + \varepsilon_{33} E_3 \end{aligned} \tag{4}$$

where s_{11}, ε_{33}, and d_{31} represent the axial elastic compliance measured with fixed electric field, the transverse dielectric constant measured with fixed stress, and the transverse-axial piezoelectric coefficient, respectively. The axial stress T_1 and the transverse electric displacement D_3 can be solved from Eq. (4)

$$\begin{aligned} T_1 &= s_{11}^{-1} S_1 - \bar{e}_{31} E_3 \\ D_3 &= \bar{e}_{31} S_1 + \bar{\varepsilon}_{33} E_3 \end{aligned} \tag{5}$$

where $\bar{e}_{31} = d_{31}/s_{11}$ and $\bar{\varepsilon}_{33} = \varepsilon_{33}(1 - k_{31}^2)$ with $k_{31}^2 = d_{31}^2/(\varepsilon_{33} s_{11})$.

The electric displacement satisfies the Gauss theorem of electrostatics

$$D_{3,3} = 0 \tag{6}$$

For the upper piezoelectric layer, the electric field E_3 and the electric potential across it can then be solved through Eqs. (1), (2), (5) and (6):

$$\begin{aligned} E_3 &= g_{31}\left(u_{3,11} x_3 - u_{1,1} - \frac{1}{2} u_{3,1}^2\right) + c_1 \\ \varphi &= -\int E_3 \mathrm{d}x_3 = -g_{31}\left(\frac{1}{2} u_{3,11} x_3^2 - u_{1,1} x_3 - \frac{1}{2} u_{3,1}^2 x_3\right) - c_1 x_3 + c_2 \end{aligned} \tag{7}$$

where $g_{31} = \bar{e}_{31}/\bar{\varepsilon}_{33}$. c_1 and c_2 are constants independent of x_3 which are determined by the electric potential boundary conditions $\varphi = 0$ at $x_3 = c$ and $\varphi = V^+$ at $x_3 = h$. The precise expressions of the electric field and of the electric displacement of the upper piezoelectric layer are thus obtained as

$$E_{3\text{upper}} = -\frac{V^+}{h-c} - \frac{g_{31}}{2}(c + h - 2x_3) u_{3,11} \tag{8}$$

$$D_{3\text{upper}} = -\frac{\bar{\varepsilon}_{33} V^+}{h-c} - \frac{\bar{e}_{31}}{2}\left[(c+h) u_{3,11} - 2u_{1,1} - u_{3,1}^2\right] \tag{9}$$

Similarly, for the lower piezoelectric layer, we have

$$E_{3\text{lower}} = \frac{V^-}{h-c} - \frac{g_{31}}{2}(c + h + 2x_3) u_{3,11} \tag{10}$$

$$D_{3\text{lower}} = \frac{\bar{\varepsilon}_{33} V^-}{h-c} - \frac{\bar{e}_{31}}{2}\left[(c+h) u_{3,11} + 2u_{1,1} + u_{3,1}^2\right] \tag{11}$$

The metallic layer in the middle is assumed to be isotropic and elastic. Hence its constitutive relation is stated as Hooke 's law

$$T_1 = E S_1 \tag{12}$$

where E is Young's modulus. The bending moment is defined by the following integral over a cross section of the beam and can be integrated explicitly with the expression for T_1 in Eqs. (5) and (12) as

$$M = \int_A x_3 T_1 \mathrm{d}x_2 \mathrm{d}x_3 = -D u_{3,11} + GV \tag{13}$$

where $D = 2[s_{11}^{-1} b(h^3 - c^3) + Ebc^3]/3$ and $G = b(h+c)\bar{e}_{31}/2$. $V = V^+ - V^-$ represents the output voltage of the harvester. The axial force F_N corresponding to stretching in the x_1 direction is defined by the following integral over the cross section of the bimorph and can be integrated using the expression for T_1 in Eqs. (5) and (12) as

$$\begin{aligned} F_N &= \int_A T_1 \mathrm{d}x_2 \mathrm{d}x_3 \\ &= f_1\left(u_{1,1} + \frac{1}{2} u_{3,1}^2\right) + b\bar{e}_{31}(V^+ + V^-) \end{aligned} \tag{14}$$

where $f_1 = 2b[s_{11}^{-1}(h-c) + Ec]$. The axial force is averaged along the length direction as

$$\begin{aligned} \bar{F}_N &= \frac{1}{L}\int_0^L F_N dx_1 \\ &= \frac{f_1}{2L}\int_0^L u_{3,1}^2 \mathrm{d}x_1 + b\bar{e}_{31}(V^+ + V^-) \end{aligned} \tag{15}$$

where boundary conditions $u_1(0,t) = u_1(L,t) = 0$ are applied. As the bimorph is driven by an external vibration, deflection is its major deformation and the in-plane displacement can be considered a higher-order effect. Therefore, the deflection and the corresponding stress components mainly need to be taken into account. The equilibrium equations for a beam under vibration with large deflection can be written as [6,7,23,24]

$$\begin{aligned} &F_{N,1} = 0 \\ &M_{,11} + (F_N u_{3,1})_{,1} + bp(x_1, t) - m\ddot{u}_3 = 0 \end{aligned} \tag{16}$$

where $m = 2\rho cb + 2\rho'(h-c)b$ is the mass per unit length of the beam, with ρ and ρ' being the mass densities of metal and ceramic, respectively. The uniform pressure $p(x_1, t) = p_0 \sin \omega_0 t$ is the load acting on the surface of the beam. A superimposed dot indicates differentiation with respect to time t.

The charge on the top electrode of the bimorph is

$$Q^+ = -b\int_0^L D_{3\text{upper}}\mathrm{d}x_1 = G\left[u_{3,1}(L,t) - u_{3,1}(0,t)\right] - \frac{\bar{e}_{31}b}{2}\int_0^L u_{3,1}^2\mathrm{d}x_1 + C_\mathrm{p}V^+ \tag{17}$$

where $C_\mathrm{p} = \bar{\varepsilon}_{33}bL/(h-c)$. The charge on the bottom electrode of the bimorph is

$$Q^- = b\int_0^L D_{3\text{lower}}\mathrm{d}x_1 = -G\left[u_{3,1}(L,t) - u_{3,1}(0,t)\right] - \frac{\bar{e}_{31}b}{2}\int_0^L u_{3,1}^2\mathrm{d}x_1 + C_\mathrm{p}V^- \tag{18}$$

The currents flowing out of the top and the bottom electrodes satisfy

$$I^+ = -\dot{Q}^+ = -I^- = \dot{Q}^- \tag{19}$$

hence

$$I^+ = -\frac{\dot{Q}^+ - \dot{Q}^-}{2} \tag{20}$$

Furthermore, the output voltage V and the output current I satisfy Ohm's law

$$I = \frac{V}{R} \tag{21}$$

where $I = I^+$. The combination of Eqs. (17), (18), (20), and (21) yields

$$V = -GR\left[\dot{u}_{3,1}(L,t) - \dot{u}_{3,1}(0,t)\right] - \frac{C_\mathrm{p}}{2}R\dot{V} \tag{22}$$

From Eqs. (17)–(19), we also have

$$C_\mathrm{p}(V^+ + V^-) - \bar{e}_{31}b\int_0^L u_{3,1}^2\mathrm{d}x_1 = 0 \tag{23}$$

It should be noticed that $V^+ + V^-$ is at most a function of the time t but does not depend on x_1. Substituting Eqs. (13)–(15), and (23) into (16) yields the equation of motion of the beam

$$Du_{3,1111} - f_2u_{3,11}\int_0^L u_{3,1}^2\mathrm{d}x_1 - bp_0\sin\omega_0 t + m\ddot{u}_3 = 0, \tag{24}$$

where $f_2 = (f_1/2L) + (\bar{e}_{31}^2b^2/C_\mathrm{p})$.

The boundary conditions for a pinned-pinned beam are

$$\begin{aligned} &u_3(0,t) = u_3(L,t) = 0 \\ &M(0,t) = M(L,t) = -Du_{3,11} + GV = 0 \end{aligned} \tag{25}$$

3 Nondimensionalization and Solutions

The solutions should satisfy the equation of motion (24) and the boundary conditions (25). Hence, we let

$$u_3(x_1,t) = w(x_1,t) + v(x_1,t) \tag{26}$$

where $w(x_1,t)$ satisfies the homogenous boundary conditions

$$\begin{aligned} &w(0,t) = w(L,t) = 0 \\ &w_{,11}(0,t) = w_{,11}(L,t) = 0 \end{aligned} \tag{27}$$

In order to meet the boundary conditions (25), we add the particular solution

$$v(x_1,t) = \frac{G}{2D}x_1(x_1 - L)V(t) \tag{28}$$

After substitution of Eq. (26), the equation of motion (24) becomes an equation for w and V

$$\ddot{w} + \frac{G}{2D}x_1(x_1-L)\ddot{V} + \frac{D}{m}w_{,1111} - \frac{f_2}{m}\left(w_{,11} + \frac{G}{D}V\right) \times \left(\int_0^L w_{,1}^2\mathrm{d}x_1 - \frac{2GV}{D}\int_0^L w\mathrm{d}x_1 + \frac{G^2L^3V^2}{12D^2}\right) - \frac{bp_0}{m}\sin\omega_0 t = 0 \tag{29}$$

Dimensionless parameters are defined as follows:

$$\bar{x}_1 = \frac{x_1}{L},\quad W = \frac{w}{h}, \bar{V} = V/\frac{Dh}{GL^2},\quad \Omega_n = \frac{\omega_n}{\omega_1},\quad \Omega_0 = \frac{\omega_0}{\omega_1},\quad \bar{t} = t\omega_1,\quad \bar{p}_0 = p_0b/mh\omega_1^2$$

where $\omega_1 = \pi^2\sqrt{D/mL^4}$. The equation of motion (29) and the circuit equation (22) become

$$\begin{aligned} &\frac{\partial^2 W}{\partial\bar{t}^2} + \frac{1}{2}\bar{x}_1(\bar{x}_1-1)\frac{\mathrm{d}^2\bar{V}}{\mathrm{d}\bar{t}^2} + \frac{D}{mL^4\omega_1^2}\frac{\partial^4 W}{\partial\bar{x}_1^4} - \bar{p}_0\sin\Omega_0\bar{t} \\ &\quad - \alpha_0\left[\frac{\partial^2 W}{\partial\bar{x}_1^2}\int_0^1\left(\frac{\partial W}{\partial\bar{x}_1}\right)^2\mathrm{d}\bar{x}_1 - 2\bar{V}\frac{\partial^2 W}{\partial\bar{x}^2}\int_0^1 W\mathrm{d}\bar{x}_1 + \frac{1}{12}\bar{V}^2\frac{\partial^2 W}{\partial\bar{x}_1^2}\right. \\ &\quad \left. + \bar{V}\int_0^1\left(\frac{\partial W}{\partial\bar{x}_1}\right)^2\mathrm{d}\bar{x}_1 - 2\bar{V}^2\int_0^1 W d\bar{x}_1 + \frac{1}{12}\bar{V}^3\right] = 0, \\ &\bar{V} = -C_0R\omega_1\left[\frac{\partial^2 W(1,\bar{t})}{\partial\bar{x}_1\partial\bar{t}} - \frac{\partial^2 W(0,\bar{t})}{\partial\bar{x}_1\partial\bar{t}}\right] - R\omega_1\left(C_0 + \frac{C_\mathrm{p}}{2}\right)\frac{\mathrm{d}\bar{V}}{\mathrm{d}\bar{t}} \end{aligned} \tag{30}$$

where $\alpha_0 = h^2f_2/mL^3\omega_1^2$, $C_0 = G^2L/D$.

Since only homogenous boundary conditions (27) are involved, $W(\bar{x}_1,\bar{t})$ can be expressed by functions with the separate variables $\bar{x}_1$ and $\bar{t}$, and can be expanded as a linear superposition of modal functions $\phi_n(\bar{x}_1)$ as

$$W(\bar{x}_1,\bar{t}) = \sum_{n=1}^{N} z_n(\bar{t})\phi_n(\bar{x}_1) \tag{31}$$

Linear modal functions $\phi_n(\bar{x}_1)$ meet the linear motion equation and homogenous boundary conditions

$$\begin{aligned} &\phi_n'''' - \lambda_n^4\phi_n = 0 \\ &\phi_n(0) = \phi_n(1) = 0,\ \phi_n''(0) = \phi_n''(1) = 0 \end{aligned} \tag{32}$$

where $\lambda_n^4 = \omega_n^2mL^4/D$. From Eq. (32), we obtain

$$\phi_n(\bar{x}_1) = \sqrt{2}\sin\lambda_n\bar{x}_1,\quad \lambda_n = n\pi,\quad n = 1,2,\ldots \tag{33}$$

Since $\int_0^1\phi_m(\bar{x}_1)\phi_n(\bar{x}_1)\mathrm{d}\bar{x}_1 = \delta_{mn}$, the modal basis is orthogonal. Substituting Eq. (31) into Eq. (30), multiplying by $\phi_n(\bar{x}_1)$ on both sides, and integrating on $\bar{x}_1$ from 0 to 1, we obtain the set of nonlinear ordinary differential equations

$$\frac{d^2 z_n}{d\bar{t}^2} - \frac{\sqrt{2}(1-\cos\lambda_n)}{\lambda_n^3}\frac{d^2\bar{V}}{d\bar{t}^2} + \Omega_n^2 z_n - \bar{p}_0 \sin(\Omega_0 \bar{t}) \int_0^1 \phi_n d\bar{x}_1 + \alpha_0 \left[\sum_{m=1}^{N}\sum_{p=1}^{N}\sum_{q=1}^{N} \int_0^1 \phi'_m \phi'_n d\bar{x}_1 \int_0^1 \phi'_p \phi'_q d\bar{x}_1 z_m z_p z_q \right.$$

$$-2\bar{V}\sum_{m=1}^{N}\sum_{p=1}^{N} \int_0^1 \phi'_m \phi'_n d\bar{x}_1 \int_0^1 \phi_p d\bar{x}_1 z_m z_p + \frac{1}{12}\bar{V}^2 \sum_{m=1}^{N} \int_0^1 \phi'_m \phi'_n d\bar{x}_1 z_m - \frac{1}{12}\bar{V}^3 \int_0^1 \phi_n d\bar{x}_1 - \bar{V} \int_0^1 \phi_n d\bar{x}_1 \sum_{p=1}^{N}\sum_{q=1}^{N} \int_0^1 \phi'_p \phi'_q d\bar{x}_1 z_p z_q$$

$$\left. + 2\bar{V}^2 \int_0^1 \phi_n d\bar{x}_1 \sum_{p=1}^{N} \int_0^1 \phi_p d\bar{x}_1 z_p \right] = 0,$$

$$\bar{V} = -R\omega_1 C_0 \sum_{m=1}^{N} [\phi'_m(1) - \phi'_m(0)] \frac{dz_m}{d\bar{t}} - R\omega_1 \left(C_0 + \frac{C_p}{2} \right) \frac{d\bar{V}}{d\bar{t}} \tag{34}$$

where ϕ'_m represents the derivative of ϕ_m with respect to the normalized coordinate $\bar{x}_1$. Equation (34) can lead to a very rich nonlinear behavior.

Since the harvester has its best harvesting efficiency when driving frequency is around the fundamental frequency, we let $N = 1$ in the following discussion. This choice enforces the fact that around resonance the fundamental mode ϕ_1 dominates the nonlinear response. After the introduction of damping, (34) becomes

$$\begin{aligned} &\frac{d^2 z_1}{d\bar{t}^2} + 2\xi\Omega_1 \frac{dz_1}{d\bar{t}} + \Omega_1^2 z_1 - \beta_1 \frac{d^2\bar{V}}{d\bar{t}^2} + \alpha_1 z_1^3 \\ &-\alpha_2 \bar{V} z_1^2 + \alpha_3 \bar{V}^2 z_1 - \alpha_4 \bar{V}^3 = F_0 \sin(\Omega_0 \bar{t}), \\ &\frac{dz_1}{d\bar{t}} - \beta_2 \frac{d\bar{V}}{d\bar{t}} - \beta_3 \bar{V} = 0 \end{aligned} \tag{35}$$

with the parameters

$$\alpha_1 = \pi^4 \alpha_0,\ \alpha_2 = 6\sqrt{2}\pi\alpha_0,\ \alpha_3 = \left(\frac{\pi^2}{12} + \frac{16}{\pi^2} \right) \alpha_0,$$

$$\alpha_4 = \frac{\sqrt{2}}{6\pi}\alpha_0,\ \beta_1 = \frac{2\sqrt{2}}{\pi^3},\ \beta_2 = \frac{1}{2\sqrt{2}\pi}\left(1 + \frac{C_p}{2C_0} \right),$$

$$\beta_3 = \frac{1}{2\sqrt{2}\pi C_0 R\omega_1},\ F_0 = \frac{2\sqrt{2}}{\pi}\bar{p}_0$$

We let

$$\begin{aligned} z_1(\bar{t}) &= U_1 \sin(\Omega_0 \bar{t}) + U_2 \cos(\Omega_0 \bar{t}), \\ \bar{V}(\bar{t}) &= V_1 \sin(\Omega_0 \bar{t}) + V_2 \cos(\Omega_0 \bar{t}) \end{aligned} \tag{36}$$

Then the harmonic balance method is employed [5–7]: We first substitute Eq. (36) into Eq. (35) and collect the coefficients of the trigonometric function. We neglect the constant terms and the higher harmonics $2\Omega_0\bar{t}$ and $3\Omega_0\bar{t}$. Finally, we let the coefficients of the sine and the cosine of $\Omega_0\bar{t}$ be zero. Thus, from Eq. (35), we obtain

$$\begin{aligned} &\frac{3}{4}(\alpha_1 U_1 - \alpha_2 V_1)|z_1|^2 + \frac{3}{4}(\alpha_3 U_1 - \alpha_4 V_1)|\bar{V}|^2 + \frac{1}{2}(\alpha_2 U_2 + \alpha_3 V_2) \\ &\times (U_2 V_1 - U_1 V_2) + \beta_1 \Omega_0^2 V_1 - 2\xi\Omega_0\Omega_1 U_2 + (\Omega_1^2 - \Omega_0^2) U_1 \\ &- F_0 = 0, \\ &\frac{3}{4}(\alpha_1 U_2 - \alpha_2 V_2)|z_1|^2 + \frac{3}{4}(\alpha_3 U_2 - \alpha_4 V_2)|\bar{V}|^2 + \frac{1}{2}(\alpha_2 U_1 + \alpha_3 V_1) \\ &\times (U_1 V_2 - U_2 V_1) + \beta_1 \Omega_0^2 V_2 + 2\xi\Omega_0\Omega_1 U_1 + (\Omega_1^2 - \Omega_0^2) U_2 = 0 \end{aligned} \tag{37}$$

where the amplitudes $|z_1|$ and $|\bar{V}|$ satisfy $|z_1|^2 = U_1^2 + U_2^2$ and $|\bar{V}|^2 = V_1^2 + V_2^2$. From (35), we have

$$\begin{aligned} &\Omega_0 U_2 - \beta_2 \Omega_0 V_2 + \beta_3 V_1 = 0, \\ &\Omega_0 U_1 - \beta_2 \Omega_0 V_1 - \beta_3 V_2 = 0 \end{aligned} \tag{38}$$

The coefficients U_1, U_2, V_1, and V_2 can be obtained by solving the nonlinear set of Eqs. (37) and (38). The output power P of the harvester is given by

$$P = \frac{\omega_0}{2\pi} \int_t^{t+2\pi/\omega_0} VI dt = \frac{D^2 h^2 (V_1^2 + V_2^2)}{2G^2 L^4 R} \tag{39}$$

4 Numerical Results and Discussion

PZT-5H is chosen as the piezoelectric material of the harvester. The metal layer is taken to be aluminum alloy. Material constants and geometric properties of the harvester are listed in Table 1 [28].

One of the main differences between a linear and a nonlinear system is that a nonlinear system can produce multiple stable steady-state solutions which are dependent on the initial conditions. A linear system in contrast always produces a unique stable solution for all initial conditions [9]. The structure we consider is a hardening oscillator, as the higher displacement curve is to the right of the linear natural frequency. For ease of discussion, we divide the frequency range near resonance of the nonlinear harvester into three regions: a left single-valued region, a multivalued region, and a right single-valued region.

A wide operation bandwidth improves the system performance of the harvester. Two methods are applied to broaden the bandwidth of the nonlinear harvester. A first one is to make the left single-valued region wider. A second one is to choose a set of initial conditions so that the largest output power can be obtained in the multivalued region.

4.1 Dependence of the Left Single-Valued Region Upon Parameters of the Nonlinear Harvester. Both analytical and numerical solutions are obtained. The numerical solutions are found by solving Eq. (35) with the Runge-Kutta method in software MATLAB. Analytical solutions are given by Eqs. (37)–(39). Figure 2 shows the dependence of the output power P with the relative driving frequency Ω_0 for different applied pressures. Near resonance, the output power becomes multivalued. Two power branches arise within the multivalued frequency region. Single-valued regions exist on its left and right sides. A jump phenomenon happens when Ω_0 exceeds a given jump-up frequency, i.e., the thin dash line J_1A for $p_0 = 10$ Pa ($\Omega_0 = 1.082$), or J_2B for $p_0 = 20$ Pa ($\Omega_0 = 1.095$), or J_3C for $p_0 = 30$ Pa ($\Omega_0 = 1.106$). This indicates that an energy-scavenging structure with optimal performance should be designed at the left single-valued region near point J_1 for $p_0 = 10$ Pa, point J_2 for $p_0 = 20$ Pa, and point J_3 for $p_0 = 30$ Pa. Otherwise, the harvester will have either a very low output power in the right single-valued region, or multiple stable steady-state output powers in the multivalued region which are

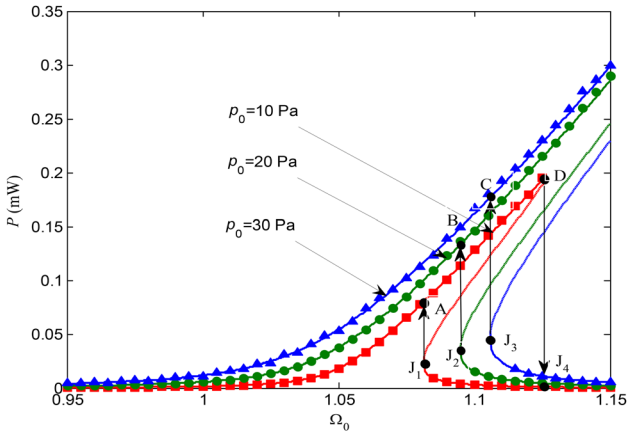

Fig. 2 Output power versus driving frequency for different applied pressures: analytical solution (solid lines) and numerical solution (■, ●, ▲)

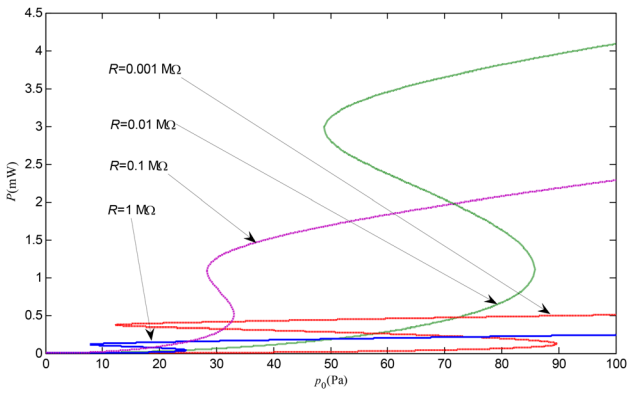

Fig. 3 Output power versus applied pressure for different electric resistors, where $\Omega_0 = 1.1$

dependent on the set of initial conditions. It is also observed that the left single-valued region expands with a larger applied pressure p_0. The performance of the harvester can be improved by widening the left single-valued region since the output power is relatively large in this region and is independent of the initial conditions.

Figure 3 shows the dependence of the output power upon the applied pressure p_0 for different electric loads, where the nondimensional driving frequency is fixed at $\Omega_0 = 1.1$. Different electric loads result in different multivalued regions as a function of the applied pressure p_0. The maximum pressure of the multivalued region decreases with increasing electric load, but the minimum pressure varies without an apparent regular pattern. Figure 4 further demonstrates the linear (lowest line) and the nonlinear output powers versus electric resistor for different applied pressures. For a small pressure of 10 Pa, a big multivalued region appears and the lower nonlinear output power is almost equal to the linear one. But for a large pressure of 30 Pa, the nonlinear output power only has a small multivalued region and is much larger than the linear output power when the resistance is larger than 20 kΩ.

In order to understand the multivalues and the jumps of the piezoelectric power harvester based on flexural vibration near resonance, we calculate the dependence of the output power P upon applied pressure p_0 for different driving frequencies Ω_0 in Fig. 5. Numerical results show that the larger Ω_0, the larger the nonlinear P-p_0 loop. Moreover, the nonlinear P-p_0 loop gradually becomes flatter as Ω_0 decreases and finally approaches a linear resonance.

A sound pressure level of 120 dB corresponds to a sound pressure of 20 Pa. It may cause hearing damage even for short-term exposure. Thus, a relatively lower applied pressure $p_0 = 10$ Pa is

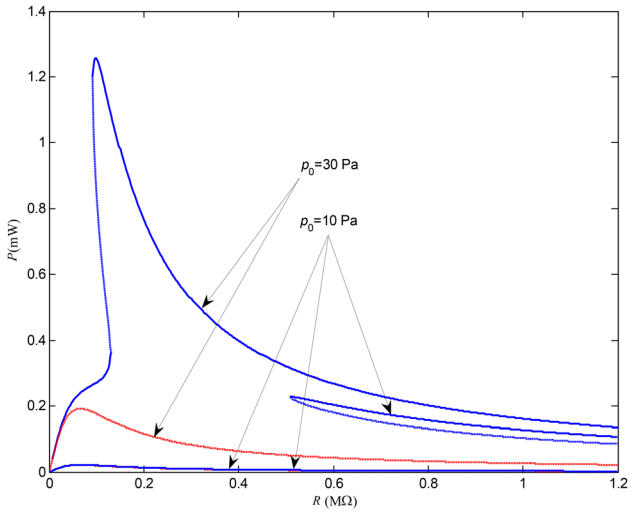

Fig. 4 Output power versus electric resistor for different applied pressures, where $\Omega_0 = 1.1$

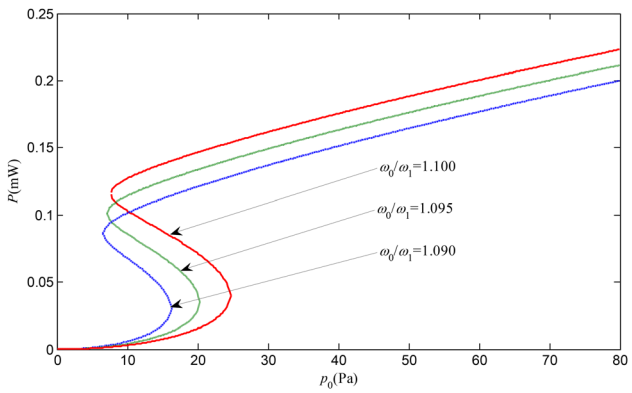

Fig. 5 Output power versus applied pressures for different Ω_0, $R = 1$ MΩ

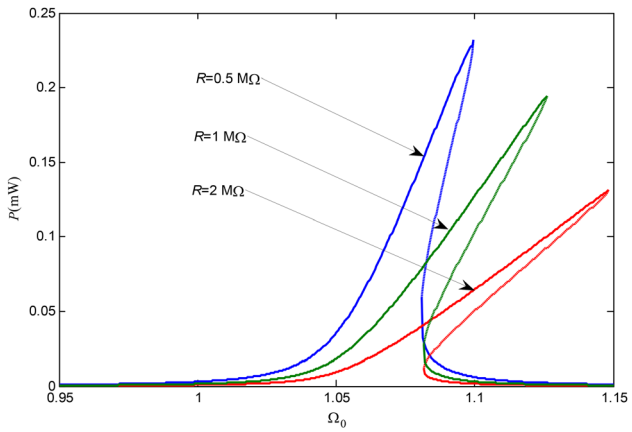

Fig. 6 Output power versus driving frequency for different electric resistors, where $p_0 = 10$ Pa

taken in the following. The dependence of the output power upon the driving frequency is plotted in Fig. 6 for different electric loads. The maximum power decreases and the jump-down frequency increases with increasing electric load. As a note, the jump-up frequency remains almost constant for different electric loads.

The linear and the nonlinear output power of the harvester versus driving frequency are shown in Fig. 7 for different span-thickness ratios l/h. The nonlinear system becomes a linear one if the nonlinearity is ignored. We practically obtain the linear result by letting α_0 be zero. This is because, based on Eq. (35), the nonlinear coefficients α_i ($i = 1, 2, 3, 4$) are equal to zero in the case that $\alpha_0 = 0$. For the linear system, the output power increases with the span-thickness ratio, but the normalized frequency corresponding to maximum power is almost the same for all span-thickness ratios. For the nonlinear system, in contrast, there exists a multivalued region. Moreover, the left single-valued region expands with an increase in the span-thickness ratio.

Figure 8 illustrates the output power of linear and nonlinear harvesters versus driving frequency for different thickness ratios h/c. For the linear system, an increase in the thickness ratio reduces the output power, but results in an increase in the normalized frequency corresponding to maximum power. For the nonlinear system, in contrast, the left single-valued region widens with a decrease in the thickness ratio.

4.2 Appropriate Initial Conditions are Imposed to Obtain a Larger Output Power. Two stable solutions exist for each frequency in the multivalued frequency range as shown by the solid lines in Fig. 2. The steady-state solution converging to the lower or the larger output power depends on initial conditions which are applied to the system. Figure 9 plots the basins of attraction to study the effect of the initial conditions on the steady-state output power of the harvester, where (a) $\Omega_0 = 1.085$, (b) $\Omega_0 = 1.105$, and (c) $\Omega_0 = 1.125$. These three frequencies locate on the starting, middle, and terminal frequencies of the multivalued region, respectively. Dark and white regions in the basin of attraction indicate that the initial conditions in the white region result in larger output power, while the initial conditions in the dark region lead to smaller output power. It can be observed that the white region shrinks and the dark region expands with increasing frequency within the multivalued region. Moreover, as seen from Fig. 9(*d*), there still remains a white region after overlapping the three basins of attraction of starting, middle, and terminal frequencies of the multivalued region. This implies that the nonlinear harvester always outputs a larger power in the whole multivalued frequency region as long as the initial conditions remain in the combined white region.

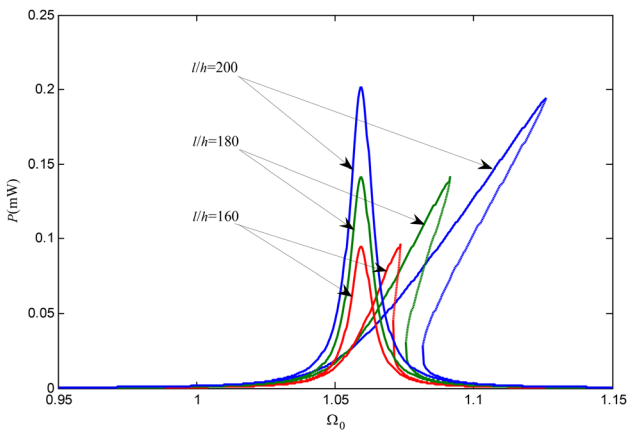

Fig. 7 Output power versus driving frequency for different span-thickness ratios l/h, where $p_0 = 10$ Pa, $R = 1$ MΩ, and $h = 0.5$ mm

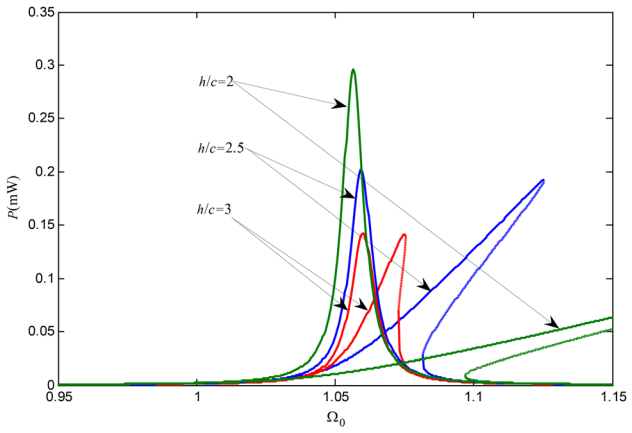

Fig. 8 Output power versus frequency for different ratios of h/c, where $p_0 = 10$ Pa, $R = 1$ MΩ, and $c = 0.2$ mm

From Eq. (31), the initial conditions for the bimorph depend on the normalized coordinate $\bar{x}_1$. Therefore, it is still difficult to impose optimal initial conditions for the whole bimorph in practice even though the optimal initial conditions $z_1(0)$ and $dz_1(0)/d\bar{t}$ are known. As a smart structure, the piezoelectric structure can be excited actively by a voltage source in order to meet a required initial condition. First, the bimorph locates the static equilibrium position. A switch then turns from the resistor to a voltage source as shown in Fig. 1(*b*) and the bimorph is excited by the harmonic voltage source $V_e \sin \omega_e t$. This excitation only needs to last for a few seconds till the bimorph vibrates from its static equilibrium position to a stable harmonic movement. The phase trajectories with $V_e = 8$V and 24 V are inserted into Fig. 9(*d*) where the frequency of the voltage source is fixed $\bar{\omega}_e = 1.08$ ($\bar{\omega}_e = \omega_e/\omega_1$). As can been seen, the phase trajectories have passed through the white region of the basins of attraction. This means that the initial conditions can be achieved by the voltage source to boost the output power of the harvester to the larger power branch in the multivalued frequency region. Moreover, it can be seen from Fig. 9(*d*) that the phase trajectory must pass through the white region if the amplitude of the bimorph $|z_1|$ is to be between 0.52 and 0.59.

Figure 10 shows the displacement amplitude of the bimorph versus the excitation frequency of the voltage source for different voltage amplitudes. To reach the displacement amplitude range between 0.52 and 0.59, the excitation voltage must be larger than 7.2 V. Besides, a different appropriate frequency range is necessary for the voltage source with different voltage amplitudes.

We can infer from Fig. 9(*d*) that only a part of the phase trajectory appears in the white region of the basin of attraction when the amplitude and the frequency of the voltage source are fixed. Therefore, it is critical to choose a suitable phase range to stop the excitation of the voltage source. Figure 11 illustrates a suitable phase range to stop the excitation of the voltage source with $\bar{\omega}_e = 1.08$, for a frequency of pressure load (a) $\Omega_0 = 1.085$, (b) $\Omega_0 = 1.105$, (c) $\Omega_0 = 1.125$, and (d) the superposition of (a), (b), and (c). After superposition, there still exists a white region of phase range. The white region of phase range means that the phase trajectories locate in the white region of the basins of attraction, i.e., the initial conditions lead to a larger output power. Therefore, the operation bandwidth of the nonlinear harvester is broadened from the left single-valued region to the whole multivalued region.

As is all known, the harvesting structure will reach a steady-state in a few seconds under the harmonic excitation. Whether the harvester outputs a lower or a larger steady-state power depends on the initial conditions. In order to obtain the larger output power in a broad frequency range, initial conditions should locate in the white region of the basin of attraction in Fig. 9(*d*). This is achieved by operating the voltage source in white region of Fig. 11(*d*).

As summarized in the flowchart of Fig. 12, imposing an optimal initial condition may include the following steps. First, design or choose a voltage source with appropriate amplitude and frequency (see Fig. 10). Second, set a voltage reference V_{ref} that the higher output voltage can attain, but that the lower one cannot. Third, switch on the voltage source (see Fig. 1(*b*)) if voltage reference has not been reached by the output voltage of the harvester within a given time interval t_{ref}. Finally, after about 2000 cycles, switch

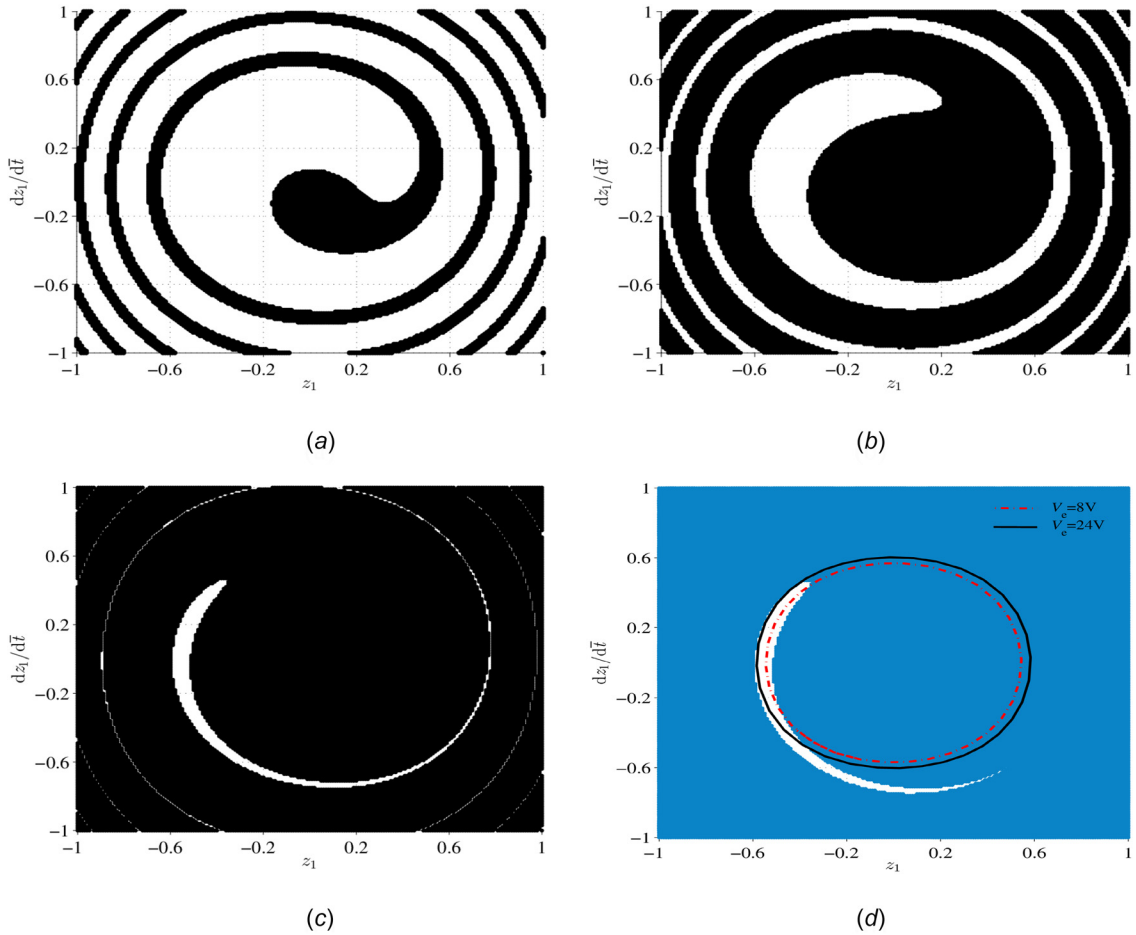

Fig. 9 Basin of attraction for the harvester with $p_0 = 10$ Pa, $R = 1$ MΩ: (*a*) $\Omega_0 = 1.085$, (*b*) $\Omega_0 = 1.105$, (*c*) $\Omega_0 = 1.125$, and (*d*) superposition of the three frequencies

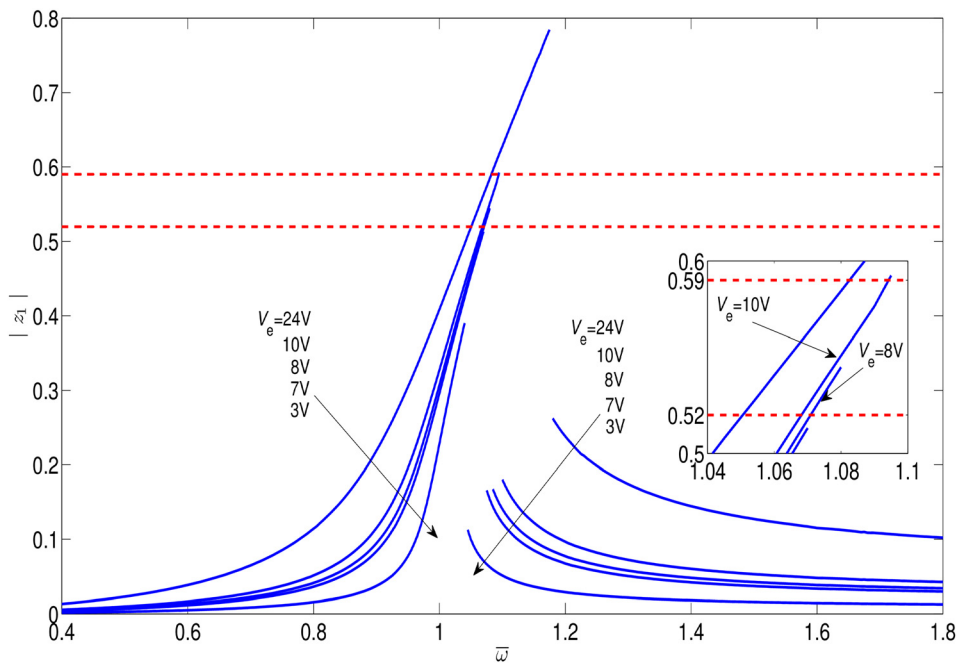

Fig. 10 Displacement amplitudes versus frequency for different excitation voltages V_e. Dotted lines limit an amplitude range for which operation is within white region of the basin of attraction in Fig. 9(*d*).

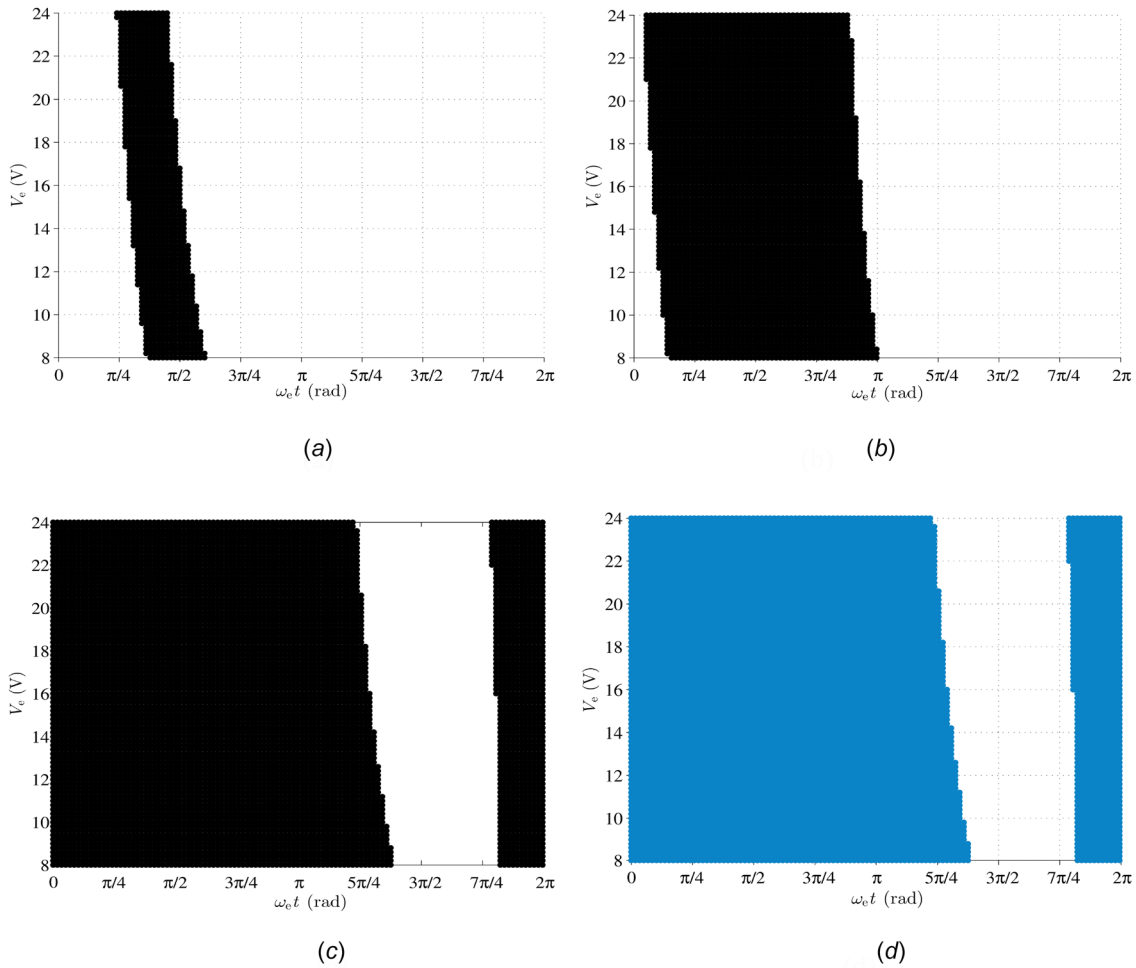

Fig. 11 Appropriate phase range to stop the excitation of the voltage source with $\bar{\omega}_e = 1.08$ and frequency of pressure load (*a*) $\Omega_0 = 1.085$, (*b*) $\Omega_0 = 1.105$, (*c*) $\Omega_0 = 1.125$, and (*d*) superposition of the three frequencies

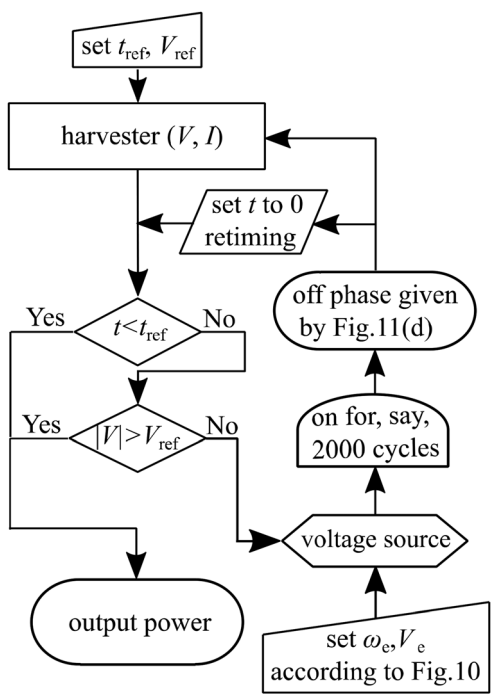

Fig. 12 Flowchart of imposing an optimal initial condition

off the voltage source and switch on the electric load at a stop phase of the exciting voltage corresponding to a white region of the basin of attraction (see Fig. 11(*d*)). The required stop phase of the voltage source can be achieved by level and sign of the voltage. The last two steps can operate in an autonomous manner.

5 Conclusions

A theoretical analysis of the performance of a nonlinear power harvester near resonance has been conducted. The basic nonlinear behavior of the harvester due to strong resonance has been predicted. The theoretical model was solved by the harmonic balance method, and analytical solutions were verified by comparison with numerical results. The dependence of the multivaluedness and jump phenomena of the output power upon applied pressure, electric load, and structural parameters was studied. These results are useful to extend the frequency span of the left single-valued region in the design of the nonlinear harvester.

Another method to broaden the operation bandwidth is to control the initial conditions of the nonlinear harvester by a voltage source to boost the output power in the multivalued region. After investigation of basins of attraction and phase trajectories, we obtained the optimal range of voltage amplitude, frequency, and phase of the voltage source. The operation bandwidth of the nonlinear harvester is broadened from the left single-valued region to the whole multivalued region.

Acknowledgment

This work was supported by the National Natural Science Foundation of China (11272126, 51435006, and 51421062), the

Fundamental Research Funds for the Central Universities, HUST: 2016JCTD114 and 2015TS121. The first author was awarded by China Scholarship Council to pursue study in France as a visiting scholar (201606165026). The authors also thank the reviewers for their meaningful comments and suggestions.

Nomenclature

A = cross section
c_1, c_2 = undetermined constants
C_0 = variable with unit as capacitance
C_p = equivalent static capacitance of the bimorph
D = equivalent bending stiffness
D_3 = electric displacement
$D_{3\text{lower}}, D_{3\text{upper}}$ = electric displacement of lower and upper piezoelectric layer
$\bar{e}_{31}$ = equivalent piezoelectric coefficient
$E_1,\ E_2, E_3$ = electric fields
$E_{3\text{lower}}, E_{3\text{upper}}$ = electric field of lower and upper piezoelectric layer
f_1, f_2 = intermediate variables
F_0 = dimensionless pressure
F_N = axial force
$\bar{F}_N$ = average axial force
g_{31} = equivalent electromechanical coupling factor
G = intermediate variables
I = output current of the harvester
I^+, I^- = currents flow out top and bottom electrodes
k_{31} = electromechanical coupling factor
M = bending moment
m = mass per unit length of the beam
N = modal order of expansion
p, p_0 = uniform pressure and its amplitude
$\bar{p}_0$ = dimensionless variable of p_0
P = output power of the harvester
Q^+, Q^- = charges on top and bottom electrodes
$t, \bar{t}$ = time, dimensionless time
t_{ref} = a given time interval
T_1 = axial stress
U_1, U_2 = amplitudes of cosine and sine parts of z_1
u_3 = flexural displacement
v = flexural displacement satisfies boundary conditions (25)
$V, |V|$ = output voltage and its amplitude of the harvester
V^-, V^+ = voltages of top and bottom electrodes
$\bar{V}, |\bar{V}|$ = dimensionless voltage and its amplitude
V_1, V_2 = amplitude of cosine and sine pars of $\bar{V}$
V_e = voltage amplitude of voltage source
V_{ref} = voltage reference
w = flexural displacement satisfies homogenous boundary conditions
W = dimensionless displacement of w
x_1, x_3 = coordinates
$\bar{x}_1$ = dimensionless coordinates
z_n = displacement function depends on $\bar{t}$
$|z_1|$ = amplitude of z_1
$\alpha\ (i = 0, 1, 2, 3, 4)$ = intermediate variables
$\beta\ (i = 1, 2, 3)$ = intermediate variables
δ_{mn} = Delta function
$\bar{\varepsilon}_{33}$ = equivalent dielectric coefficient
λ_n = characteristic root
φ = electric potential
ϕ_n = linear modal functions
Ω_n = dimensionless frequency of ω_n
ω_0 = driving frequency of ambient vibration
ω_e = angular frequency of voltage source
ω_n = modal frequency

References

[1] Roundy, S., Wright, P. K., and Rabaey, J., 2003, "A Study of low Level Vibrations as a Power Source for Wireless Sensor Nodes," Comput. Commun., **26**(11), pp. 1131–1144.
[2] Yang, J. S., Chen, Z. G., Hu, Y. T., Jiang, S. N., and Guo, S. H., 2007, "Weakly Nonlinear Behavior of a Plate Thickness-Mode Piezoelectric Transformer," IEEE Trans. Ultrason. Ferroelectr. Freq. Control, **54**(4), pp. 877–881.
[3] Hu, Y. T., Xue, H., Hu, T., and Hu, H. P., 2008, "Nonlinear Interface Between the Piezoelectric Harvesting Structure and the Modulating Circuit of an Energy Harvester With a Real Storage Battery," IEEE Trans. Ultrason. Ferroelectr. Freq. Control, **55**(1), pp. 148–160.
[4] Liang, J., and Liao, W. H., 2011, "Energy Flow in Piezoelectric Energy Harvesting Systems," Smart Mater. Struct., **20**(1), p. 015005.
[5] Hu, Y. T., Xue, H., Yang, J. S., and Jiang, Q., 2006, "Nonlinear Behavior of a Piezoelectric Power Harvester Near Resonance," IEEE Trans. Ultrason. Ferroelectr. Freq. Control, **53**(7), pp. 1387–1391.
[6] Xue, H., and Hu, H. P., 2008, "Nonlinear Characteristics of a Circular Plate Piezoelectric Harvester With Relatively Large Deflection Near Resonance," IEEE Trans. Ultrason. Ferroelectr. Freq. Control, **55**(9), pp. 2092–2096.
[7] Wang, H. R., Xie, J. M., Hu, Y. T., and Wang, J., 2014, "Nonlinear Characteristics of Circular-Cylinder Piezoelectric Power Harvester Near Resonance Based on Flow-Induced Flexural Vibration Mode," Appl. Math. Mech., **35**(2), pp. 229–236.
[8] Wang, H. R., Xie, X., Hu, Y. T., and Wang, J., 2013, "Weakly Nonlinear Characteristics of a Three-Layer Circular Piezoelectric Plate-Like Power Harvester Near Resonance," J. Mech., **30**(1), pp. 97–102.
[9] Ramlan, R., Brennan, M., Mace, B., and Kovacic, I., 2010, "Potential Benefits of a Non-Linear Stiffness in an Energy Harvesting Device," Nonlinear Dyn., **59**(4), pp. 545–558.
[10] Wu, H., Tang, L., Yang, Y., and Soh, C. K., 2014, "Development of a Broadband Nonlinear Two-Degree-of-Freedom Piezoelectric Energy Harvester," J. Intell. Mater. Syst. Struct., **25**(14), pp. 1875–1889.
[11] Barton, D. A. W., Burrow, S. G., and Clare, L. R., 2010, "Energy Harvesting From Vibrations With a Nonlinear Oscillator," ASME J., Vib. Acoust., **132**(2), p. 021009.
[12] Leadenham, S., and Erturk, A., 2015, "Nonlinear M-Shaped Broadband Piezoelectric Energy Harvester for Very Low Base Accelerations: Primary and Secondary Resonances," Smart Mater. Struct., **24**(5), p. 055021.
[13] Yang, Z., Zhu, Y., and Zu, J., 2015, "Theoretical and Experimental Investigation of a Nonlinear Compressive-Mode Energy Harvester With High Power Output Under Weak Excitations," Smart Mater. Struct., **24**(2), p. 025028.
[14] Stanton, S. C., McGehee, C. C., and Mann, B. P., 2010, "Nonlinear Dynamics for Broadband Energy Harvesting: Investigation of a Bistable Piezoelectric Inertial Generator," Physica D, **239**(10), pp. 640–653.
[15] Harne, R., and Wang, K., 2013, "A Review of the Recent Research on Vibration Energy Harvesting Via Bistable Systems," Smart Mater. Struct., **22**(2), p. 023001.
[16] Pellegrini, S. P., Tolou, N., Schenk, M., and Herder, J. L., 2012, "Bistable Vibration Energy Harvesters: A Review," J. Intell. Mater. Syst. Struct., **24**(11), pp. 1303–1312.
[17] Masana, R., and Daqaq, M. F., 2012, "Energy Harvesting in the Super-Harmonic Frequency Region of a Twin-Well Oscillator," J. Appl. Phys., **111**(4), p. 044501.
[18] Hu, H. P., Xue, H., and Hu, Y. T., 2007, "A Spiral-Shaped Harvester With an Improved Harvesting Element and an Adaptive Storage Circuit," IEEE Trans. Ultrason. Ferroelectr. Freq. Control, **54**(6), pp. 1177–1187.
[19] Jiang, S. N., and Hu, Y. T., 2007, "Analysis of a Piezoelectric Bimorph Plate With a Central-Attached Mass as an Energy Harvester," IEEE Trans. Ultrason. Ferroelectr. Freq. Control, **54**(7), pp. 1463–469.
[20] Wang, H. R., Hu, H. P., Yang, J. S., and Hu, Y. T., 2013, "Spiral Piezoelectric Transducer in Torsional Motion as Low-Frequency Power Harvester," Appl. Math. Mech., **34**(5), pp. 589–596.
[21] Wang, Y. J., Lian, Z. Y., Wang, J., and Hu, H. P., 2013, "Analysis of a Piezoelectric Power Harvester With Adjustable Frequency by Precise Electric Field Method," IEEE Trans. Ultrason. Ferroelectr. Freq. Control, **60**(10), pp. 2154–2161.
[22] Reddy, J. N., 2004, *Mechanics of Laminated Composite Plates and Shells: Theory and Analysis*, CRC Press, London.
[23] Eisley, J. G., 1964, "Nonlinear Vibration of Beams and Rectangular Plates," Z. Angew. Math. Phys., **15**(2), pp. 167–175.
[24] Pirbodaghi, T., Fesanghary, M., and Ahmadian, M., 2011, "Non-Linear Vibration Analysis of Laminated Composite Plates Resting on Non-Linear Elastic Foundations," J. Franklin Inst. Eng. Appl. Math., **348**(2), pp. 353–368.
[25] Xie, J. M., Yang, J. S., Hu, H. P., Hu, Y. T., and Chen, X. D., 2012, "A Piezoelectric Energy Harvester Based on Flow-Induced Flexural Vibration of a Circular Cylinder," J. Intell. Mater. Syst. Struct., **23**(2), pp. 135–139.
[26] Yang, J. S., and Fang, H. Y., 2002, "Analysis of a Rotating Elastic Beam With Piezoelectric Films as an Angular Rate Sensor," IEEE Trans. Ultrason. Ferroelectr. Freq. Control, **49**(6), pp. 798–804.
[27] Meitzler, A., Tiersten, H., Warner, A., Berlincourt, D., Coquin, G., and Welsh, F., III, 1988, "IEEE Standard on Piezoelectricity," American National Standards Institute, New York.
[28] Auld, B. A., 1973, *Acoustic Fields and Waves in Solids*, Wiley, New York.